machines

MDPI

Article

Rotor-Driven Blade Rotor Volumetric Pump: Enhanced Stability and Flow Uniformity via Kinematic Optimization

Yuanping He [1,2], Feifei Zhao [1,*], Bin Lin [2,*], Tianyi Sui [2], Liang Fang [1] and Xingfu Hong [1]

[1] High Speed Aerodynamics Institute, China Aerodynamics Research and Development Center, Mianyang 621000, China; tdhyp2013@tju.edu.cn (Y.H.); fangliang_26@cardc.cn (L.F.); hxfhsy@163.com (X.H.)
[2] Key Laboratory of Advanced Ceramics and Machining Technology, Ministry of Education, Tianjin University, Tianjin 300350, China; suity@tju.edu.cn
* Correspondence: zfftju2016@163.com (F.Z.); linbin@tju.edu.cn (B.L.)

Abstract

The Blade Rotor Volumetric Pump (BRVP) integrates the operational advantages of vane pumps and positive displacement pumps, enabling a single unit to efficiently achieve both a high flow rate and a high head. This represents a significant expansion of the existing pump design spectrum. However, performance testing of the initial Blade-Driven BRVP (BD-BRVP) prototype revealed critical challenges requiring resolution, including the absence of established design theory and unsatisfactory operational smoothness. This study presents a comprehensive analysis of the BD-BRVP's design principles, mechanical system, and flow characteristics, grounded in the kinematics of a rotationally symmetric crank-guide rod mechanism. Building on this analysis, we propose an innovative Rotor-Driven BRVP (RD-BRVP) configuration. Our results demonstrate that the RD-BRVP significantly outperforms the BD-BRVP in force transmission efficiency and operational smoothness. Specifically, the RD-BRVP exhibits a 42.5% reduction in rotational speed fluctuation and a 20.75% decrease in flow pulsation rate compared to the BD-BRVP. These performance enhancements are conclusively validated through experimental testing. This research advances the technological maturity of the BRVP concept and establishes a foundation for its future practical deployment.

Keywords: Blade Rotor Volumetric Pump (BRVP); crank-guide rod; flow pulsation; operational smoothness; pump design

check for updates

Academic Editor: Davide Astolfi

Received: 11 August 2025
Revised: 7 September 2025
Accepted: 10 September 2025
Published: 11 September 2025

Citation: He, Y.; Zhao, F.; Lin, B.; Sui, T.; Fang, L.; Hong, X. Rotor-Driven Blade Rotor Volumetric Pump: Enhanced Stability and Flow Uniformity via Kinematic Optimization. *Machines* **2025**, *13*, 843. https://doi.org/10.3390/machines13090843

Copyright: © 2025 by the authors. Licensee MDPI, Basel, Switzerland. This article is an open access article distributed under the terms and conditions of the Creative Commons Attribution (CC BY) license (https://creativecommons.org/licenses/by/4.0/).

1. Introduction

Pumps constitute indispensable industrial equipment, extensively employed across critical sectors of the national economy and human activities, including aerospace, nuclear power generation, municipal water supply, and petrochemical processing [1,2]. Statistical analyses reveal a significant energy footprint: pump systems account for approximately 20% of global electricity usage, contributing to roughly 5% of total national energy consumption. This substantial energy demand underscores the critical imperative for advancements in pump technology to enhance energy efficiency [3,4]. Beyond energy consumption, reliability and stability under high-pressure conditions are critical performance metrics for industrial pumps, particularly in applications where failure can lead to significant operational downtime or safety hazards.

Pumps are fundamentally categorized by their operating principle into two primary types: vane pumps and positive displacement pumps. Vane pumps (e.g., centrifugal

pumps) transfer energy through dynamic interactions between fluid and rotating blades, enabling high flow rates but typically limited to low- to medium-pressure applications due to inherent leakage paths and reduced volumetric efficiency at elevated pressures [5]. Conversely, positive displacement pumps (e.g., plunger pumps) operate via cyclic variations in enclosed chamber volumes, capable of generating very high pressures but often at the expense of lower flow rates and higher flow pulsation, which can induce vibration and noise [6,7]. Current research efforts focus on overcoming these inherent limitations through several primary optimization strategies: (1) structural enhancements, such as novel impeller geometries or optimized volute designs, aiming to improve hydraulic efficiency and reduce erosion [8,9]; (2) advanced materials, including ceramics and composites, to enhance wear resistance and durability under abrasive conditions [10]; (3) multi-stage configurations, which stack multiple pumping elements to achieve higher heads, albeit with increased complexity, cost, and axial length [11,12]; and (4) intelligent control systems [13], designed to optimize pump operation in real-time based on demand, improving system-level efficiency. International research efforts increasingly leverage computational fluid dynamics (CFD) simulations coupled with experimental validation to improve hydraulic efficiency and operational durability [8]. Despite these advancements, a significant technological challenge remains: the development of a single-stage pump architecture capable of simultaneously delivering both high flow rates and high heads without compromising operational stability or efficiency [14,15].

Recent attempts to create hybrid or novel pump designs that bridge this performance gap have been explored. For instance, Hsieh et al. proposed a novel variable clearance design for cycloidal pumps, which reduces collisions between components. An appropriately designed variable clearance maintains robust flow characteristics, effectively minimizes impact and collision among pump parts, thereby lowering stress levels, improving stability, and extending the service life of cycloidal pumps [16]. Li et al. proposed a novel alternating flow (AF) variable displacement hydraulic pump designed to eliminate metering losses by acting as a high-bandwidth pump for displacement control, achieve high efficiency under various operating conditions and displacements, and enable the compact integration of multiple units on a single prime mover shaft for multi-actuator displacement control systems [17]. These approaches highlight the persistent difficulty in achieving a compact, efficient, and reliable design that truly bridges the performance gap.

Addressing this challenge, the Blade-Driven Blade Rotor Volumetric Pump (BD-BRVP), developed by Tianjin University's Key Laboratory of Advanced Ceramics and Processing Technology [18,19], integrates the advantageous principles of both vane and positive displacement pumps. This novel configuration fundamentally differs from the aforementioned hybrid approaches by utilizing a single working chamber with coordinated blade and rotor kinematics, thereby avoiding the complications of multi-stage integration. The main parameters governing our design include the eccentricity and the blade-rotor phase relationship, which collectively enable a single stage to achieve high flow and high head simultaneously. This innovative design enables a single pump unit to achieve high flow rates, elevated heads, high power density, and peak efficiency through the coordinated action of structural volume variations and blade rotations. However, performance evaluations of first-generation Blade-Driven BRVP (BD-BRVP) prototypes exposed critical limitations, notably running instability (manifesting as Grade D vibration severity of 28 mm/s) and a lack of comprehensive theoretical design models, which constrained overall performance and increased operational risks. This instability was primarily attributed to its complex force-flow transmission path and significant flow pulsation.

To overcome these limitations, the present study undertakes a systematic investigation of the BD-BRVP, encompassing: (1) kinematic analysis of the BD-BRVP based on a

rotationally symmetric crank-guide rod mechanism; (2) mechanical system optimization focusing on force transmission paths, and (3) proposal and experimental validation of a redesigned Rotor-Driven BRVP (RD-BRVP) configuration. Building upon this foundational analysis, the RD-BRVP is proposed and evaluated. Experimental results confirm the efficacy of this redesign, demonstrating a 42.5% reduction in rotational speed fluctuation and a 20.75% decrease in flow pulsation compared to the BD-BRVP. These advancements provide both essential theoretical foundations and robust technical support for the development of next-generation volumetric pumps.

2. Structure and Working Principle of BRVP

As illustrated in Figure 1, the Blade Rotor Volumetric Pump (BRVP) incorporates the following key components: a drive blade, two driven blades, a rotor, three sliders, and a splined drive shaft. The rotor and blades are eccentrically arranged relative to their respective rotational centers. The drive blade is operatively connected to the power input shaft via the splined drive shaft. Sliders are housed within dedicated grooves on the rotor. During operation, the drive blade simultaneously actuates the sliders and the rotor. The rotor, in turn, drives the two driven blades, thereby enabling the complete mechanism's motion.

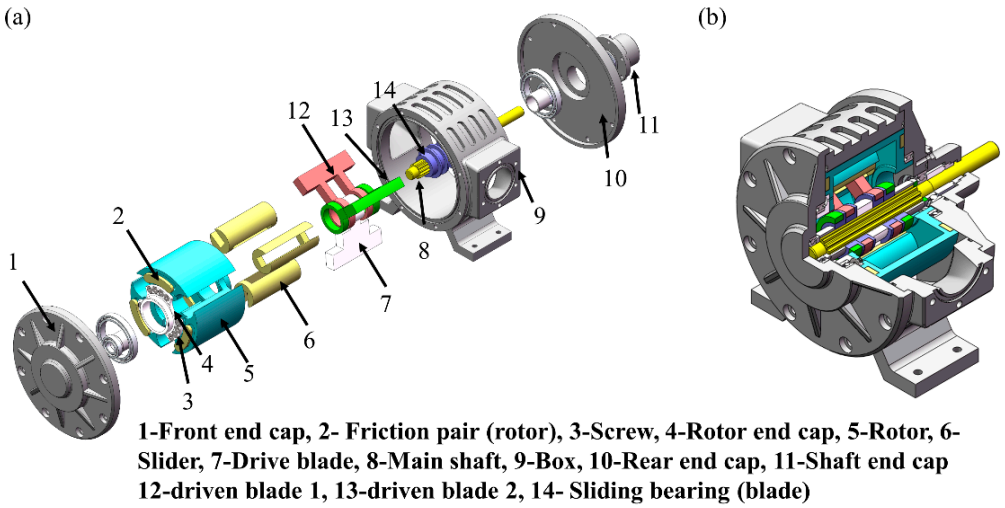


Figure 1. 3D model of the BD-BRVP: (**a**) explosive model; (**b**) semi-sectional model.

Energy conversion within the BRVP occurs through the interaction between the rotating blades and the working fluid, transforming mechanical input energy into hydraulic energy (increased fluid pressure and kinetic energy). During blade rotation, the working chamber volume at the inlet progressively expands, creating a partial vacuum that continuously draws fluid into the pump. Concurrently, the working chamber volume at the outlet progressively contracts, generating a high-pressure zone that discharges the fluid. Reversing the input power direction causes all components to operate in reverse sequence, effectively swapping the inlet and outlet functions to provide bidirectional pumping capability.

Kinematically, the BRVP mechanism can be represented as a rotationally symmetric crank-guide rod mechanism (See Figure 2). In this analogy,

- The rotor functions as three rigid cranks fixed at 120° intervals;
- The three blades function as the guide rods;
- One blade serves as the driving element;
- Three sliders are integrated into the rotor's grooves;

- The rotational centers of the blades (rods) and the rotor (cranks) maintain a fixed eccentric arrangement.

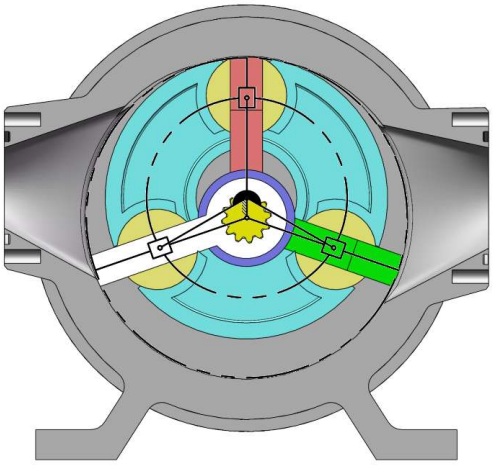


Figure 2. Structural and motion diagram of the BRVP.

Within the BRVP, the three blades share a common, fixed rotational center. This configuration ensures a constant distance between each blade tip and its rotational center, equivalent to the blade length, throughout the entire operational cycle. This relative motion among components enables the equivalent of "reciprocating motion" in vane pumps (typically achieved through centrifugal forces and hydraulic pressure). This kinematic design significantly enhances mechanism stability and operational reliability while eliminating the requirement for dynamic sealing elements.

The blade structural design demands sufficient strength and stiffness solely to prevent fluid leakage caused by blade deformation under high working pressure differentials. A clearance sealing mechanism between the blades and the housing is achieved through precision tolerance matching. This approach effectively resolves the persistent vane wear issues common in conventional vane pumps.

Consequently, BRVP retains the performance advantages of vane pumps while resolving their inherent limitations through optimized mechanical configuration. Specifically, it mitigates vane and stator wear, thermal losses, and excessive power consumption, thereby achieving the design objectives of enhanced operational efficiency and extended service life.

3. BD-BRVP Mechanical System Analysis and Flow Characteristics

3.1. BD-BRVP Mechanical System Analysis

(1) Kinematic analysis

(i) Angular velocities and relative velocities of BD-BRVP components

The kinematic schematic of the BD-BRVP mechanism is illustrated in Figure 3. Component 1 represents the drive blade, while components $1'$ and $1''$ represent driven blades of radius R rotating about center O. Component 3 denotes the rotor of radius (R-e) rotating about center O_1. Components 2, $2'$, and $2''$ correspond to sliders of radius r, interfacing with blades 1, $1'$, and $1''$, respectively. The eccentricity e is defined as the distance between the rotational centers O (blades) and O_1 (rotor). Component 4 represents the stationary frame. A Cartesian coordinate system is established with origin at blade rotational center O, where the eccentricity vector aligns with the positive Y-axis. The solid lines, dashed lines, and dot-dashed lines represent the initial position, the position after the rotation of the drive blade, and the trajectories, respectively. Accordingly, Points A, B, and C correspond to the tip positions of the three blades after rotation. The vector orientations and angular relationships are annotated in Figure 3.

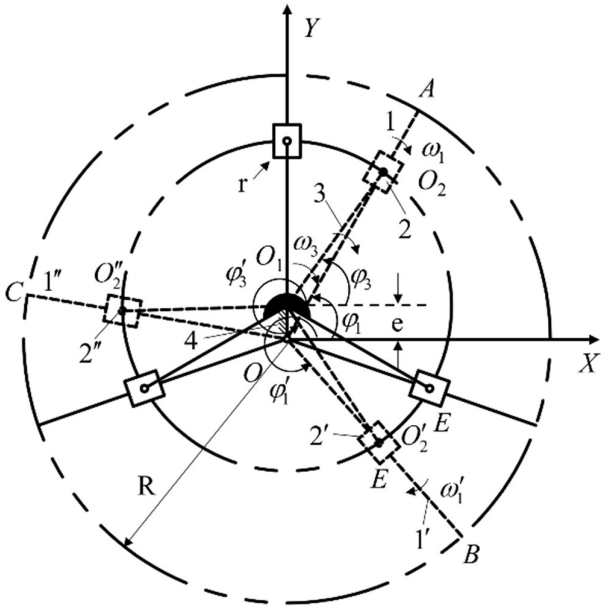


Figure 3. Schematic diagram of the motion of the BD-BRVP (clockwise).

From the vector triangle ΔOO_1O_2 in Figure 3, the following relationship can be derived:

$$e\mathbf{e}^{i\pi/2} + (R - r - e)\mathbf{e}^{i\varphi_3} = l_{OO_2}\mathbf{e}^{i\varphi_1} \tag{1}$$

where φ_1 and φ_3 represent the angular displacements of drive blade 1 and rotor 3, respectively.

The angular velocity of the rotor ω_3 can be obtained from Equation (1):

$$\omega_3 = \frac{l_{OO_2}\omega_1}{(R - r - e)\cos(\varphi_1 - \varphi_3)} \tag{2}$$

where

$$\varphi_1 = \varphi_3 + \arcsin\tfrac{e\cos\varphi_1}{R-r-e}$$

$$l_{OO_2} = \sqrt{(R - r - e)^2 + e^2 + 2e(R - r - e)\sin(\varphi_1 - \varphi_3)}$$

Similarly, the angular velocities of driven blades ω_1' and ω_1'' are calculated as:

$$\omega_1' = \frac{\omega_3(R - r - e)\cos(\varphi_3' - \varphi_1')}{l_{OO_2'}} \tag{3}$$

$$\omega_1'' = \frac{\omega_3(R - r - e)\cos(\varphi_3'' - \varphi_1'')}{l_{OO_2''}} \tag{4}$$

where

$$\varphi_3' = \varphi_3 + \tfrac{4}{3}\pi$$
$$\varphi_1' = \arctan\left(\tfrac{e+(R-r-e)\sin\varphi_3'}{(R-r-e)\cos\varphi_3'}\right)$$
$$l_{OO_2'} = \sqrt{(R - r - e)^2 + e^2 + 2e(R - r - e)\sin\varphi_3'}$$
$$\varphi_3'' = \varphi_3 + \tfrac{2}{3}\pi$$
$$\varphi_1'' = \arctan\left(\tfrac{e+(R-r-e)\sin\varphi_3''}{(R-r-e)\cos\varphi_3''}\right)$$
$$l_{OO_2''} = \sqrt{(R - r - e)^2 + e^2 + 2e(R - r - e)\sin\varphi_3''}$$

The relative angular displacement between sliders and their grooves is $\beta = \angle OO_2O_1 = \arcsin(\frac{e\cos\varphi_1}{R-r-e})$. By differentiating β with respect to time t, the relative angular velocity ω_2 is determined:

$$\omega_2 = -\frac{e\sin\varphi_1}{\sqrt{(R-r-e)^2-(e\cos\varphi_1)^2}}\omega_1 \tag{5}$$

(2) Dynamic analysis

(i) Working resistance torque calculation

Assuming a constant operational pressure differential ($\Delta p = p_o - p_i$, where p_i is the inlet pressure and p_o is the outlet pressure), the working resistance torque on the blades is primarily dependent on their projection length l_{BE}, which varies with the blade's angular position.

(a) Let position Y denote the initial reference position of drive blade 1. When the drive blade rotates through an angle θ, for analytical simplification, define: $\alpha_0 = \arcsin\left(\frac{\sqrt{3}(R-e-r)}{2\sqrt{e^2+(R-e-r)^2-e(R-e-r)}}\right)$, At $\theta \in (0, \pi-\alpha_0)$ ($\theta = \pi/2 + 2k\pi - \varphi$), driven blade 1′ enters the operational state. The working resistance torque M'_{r1} acting on driven blade 1′ is expressed as:

$$M'_{r1} = eL(p_o-p_i)(R-e)\cdot\left(1+\cos\left(\begin{array}{c}\arcsin\left(\frac{e(R-r-e)\sin(\frac{\pi}{3}-\theta-\beta)}{(R-e)\sqrt{(R-r-e)^2+e^2-2e(R-r-e)\cos(\frac{\pi}{3}-\theta-\beta)}}\right)\\ -\arcsin\left(\frac{(R-r-e)\sin(\frac{\pi}{3}-\theta-\beta)}{\sqrt{(R-r-e)^2+e^2-2e(R-r-e)\cos(\frac{\pi}{3}-\theta-\beta)}}\right)\end{array}\right)\right) \tag{6}$$

(b) When drive blade 1 rotates to angle θ ($\theta \in (\pi-\alpha_0, \pi+\alpha_0)$), it assumes primary operational status. The working resistance torque M_{r1} acting on the drive blade is formulated as:

$$M_{r1} = eL(p_o-p_i)(R-e)\left(1+\cos\left(\theta+\arcsin\left(\frac{e\sin\theta}{R-e}\right)\right)\right) \tag{7}$$

(c) When drive blade 1 rotates to angle θ ($\theta \in (\pi+\alpha_0, 2\pi)$), driven blade 1″ enters the operational state. The working resistance torque M''_{r1} acting on the drive blade is formulated as:

$$M''_{r1} = eL(p_o-p_i)(R-e)\cdot\left(1+\cos\left(\begin{array}{c}\arcsin\left(\frac{e(R-r-e)\sin(\frac{\pi}{3}+\theta+\beta)}{(R-e)\sqrt{(R-r-e)^2+e^2-2e(R-r-e)\cos(\frac{\pi}{3}+\theta+\beta)}}\right)\\ -\arcsin\left(\frac{(R-r-e)\sin(\frac{\pi}{3}+\theta+\beta)}{\sqrt{(R-r-e)^2+e^2-2e(R-r-e)\cos(\frac{\pi}{3}+\theta+\beta)}}\right)\end{array}\right)\right) \tag{8}$$

(ii) Driveshaft driving torque calculation (inertial effects neglected)

Under the assumption of negligible inertial forces/moments, energy transmission losses, and frictional dissipation, the three blades operate sequentially with only one blade

active at any instant during a full rotation cycle. The driveshaft driving torque M is derived as:

$$M = \begin{cases} M'_{r1} n'_1 / n_1 & \theta \in (0, \pi - \alpha_0) \\ M_{r1} & \theta \in (\pi - \alpha_0, \pi + \alpha_0) \\ M''_{r1} n''_1 / n_1 & \theta \in (\pi + \alpha_0, 2\pi) \end{cases} \tag{9}$$

(iii) Driveshaft driving torque with inertial effects

Figure 4 illustrates the force diagram of BD-BRVP incorporating inertial forces and moments. Assuming negligible gravitational, inertial, and moment effects from slider 2 due to its minimal mass, the driving torque M is formulated as:

$$\begin{aligned} &M_{I3}\omega_3 + (M_{I1} + M_{r1} + M)\omega_1 + (M'_{I1} + M'_{r1})\omega'_1 + (M''_{I1} + M''_{r1})\omega''_1 + (G_1 + F_{I1y})v_{S_1 y} \\ &+(G'_1 + F'_{I1y})v'_{S'_1 y} + (G''_1 + F''_{I1y})v''_{S''_1 y} + F_{I1x}v_{S_1 x} + F'_{I1x}v'_{S'_1 x} + F''_{I1x}v''_{S''_1 x} + (G_3 + F_{I3y})v_{S_3 y} + F_{I3x}v_{S_3 x} = 0 \end{aligned} \tag{10}$$

where M_{I1} is the inertial moment of the drive blade 1; F_{I1y} is the inertial force along the y-direction at the center of mass of the drive blade 1; $v_{S_1 y}$ is the velocity along the y-direction at the center of mass of the drive blade 1; G'_1 is the gravity at the center of mass of the driven blade 1′.

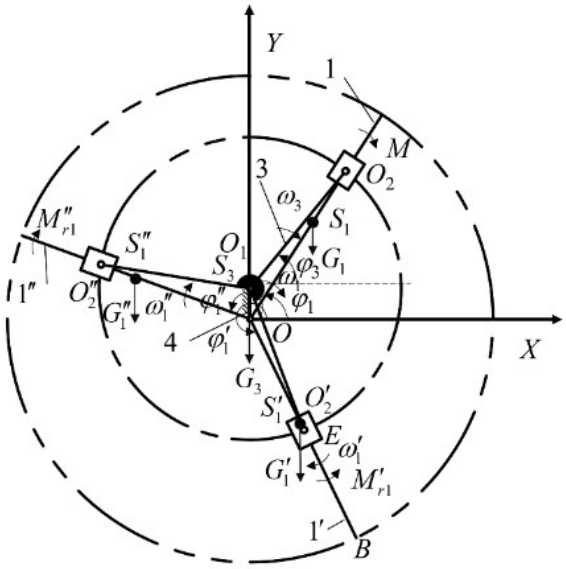


Figure 4. Schematic diagram of the force on the BD-BRVP.

(a) When $\varphi \in (0, \frac{\pi}{2}) \cup (\alpha_0 + \frac{3\pi}{2}, 2\pi)$, $M''_{r1} = 0$, $M_{r1} = 0$, then

$$M = -\frac{1}{\omega_1}\left(\begin{array}{l} M_{I3}\omega_3 + (M'_{I1} + M'_{r1})\omega'_1 + M''_{I1}\omega''_1 + (G_1 + F_{I1y})v_{S_1 y} \\ +(G'_1 + F'_{I1y})v'_{S'_1 y} + (G''_1 + F''_{I1y})v''_{S''_1 y} + F_{I1x}v_{S_1 x} + F'_{I1x}v'_{S'_1 x} + F''_{I1x}v''_{S''_1 x} \end{array} \right) \tag{11}$$

(b) When $\varphi \in (\frac{3\pi}{2} - \alpha_0, \alpha_0 + \frac{3\pi}{2})$, $M''_{r1} = 0$, $M'_{r1} = 0$, then

$$M = -\frac{1}{\omega_1}\left(\begin{array}{l} M_{I3}\omega_3 + M'_{I1}\omega'_1 + M''_{I1}\omega''_1 + (G_1 + F_{I1y})v_{S_1 y} + (G'_1 + F'_{I1y})v'_{S'_1 y} \\ +(G''_1 + F''_{I1y})v''_{S''_1 y} + F_{I1x}v_{S_1 x} + F'_{I1x}v'_{S'_1 x} + F''_{I1x}v''_{S''_1 x} \end{array} \right) - M_{r1} \tag{12}$$

(c) When $\varphi \in (\frac{\pi}{2}, \frac{3\pi}{2} - \alpha_0)$, $M_{r1} = 0$, $M'_{r1} = 0$, then

$$M = -\frac{1}{\omega_1}\left(\begin{array}{l} M_{I3}\omega_3 + M'_{I1}\omega'_1 + (M''_{I1} + M''_{r1})\omega''_1 + (G_1 + F_{I1y})v_{S_1 y} + (G'_1 + F'_{I1y})v'_{S'_1 y} \\ +(G''_1 + F''_{I1y})v''_{S''_1 y} + F_{I1x}v_{S_1 x} + F'_{I1x}v'_{S'_1 x} + F''_{I1x}v''_{S''_1 x} \end{array} \right) \tag{13}$$

3.2. BRVP Flow Characteristics Analysis

(1) Mean Flow Rate

Figure 5 shows the schematic for calculating BRVP's mean flow rate. Defining the geometric references: O represent the main shaft center, O_1 denote the rotor center, and O_2 indicate the slider center. The displacement q of BRVP is defined as

$$q = 3S_{BECF}L \tag{14}$$

$$S_{BECF} = S_{BOC} - S_{E'O_1F'} + 2S_{\Delta O_2'O_1O} - 2S_{O_2EE'} \tag{15}$$

$$S_{BECF} = (\alpha_0 + \frac{\pi}{3})R^2 - \frac{\pi}{3}(R-e)^2 + \frac{\sqrt{3}}{2}e(R-e-r) - r^2\alpha_0 \tag{16}$$

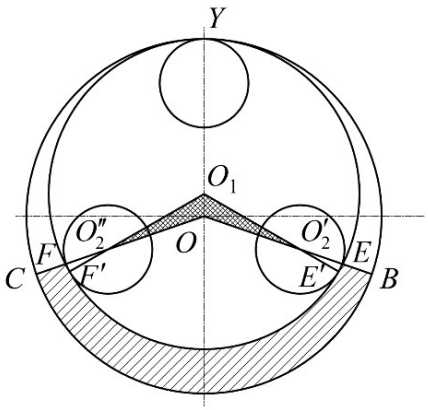


Figure 5. Diagram for calculating the average flow rate of the BRVP.

The theoretical mean flow rate $\overline{Q}$ is given by:

$$\overline{Q} = qn = 3S_{BECF}Ln_1 \tag{17}$$

(2) Instantaneous Flow Characteristics

(i) BD-BRVP Instantaneous Flow Calculation (Blade Thickness Neglected)

Figure 6 presents the BD-BRVP schematic, where discharged liquid volume varies with drive blade rotation angle θ. Instantaneous flow rate calculation over one complete drive blade revolution comprises three discrete phases:

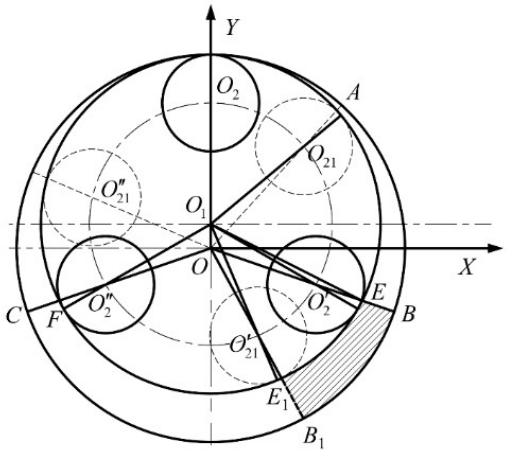


Figure 6. Schematic diagram of instantaneous flow calculation for BD-BRVP without considering blade thickness.

(a) When the drive blade rotates through an angle $\theta < \pi - \alpha_0$, driven blade $1'$ enters the operational state. To simplify the calculation, the influence of blade thickness on instantaneous flow rate is neglected. As the drive blade rotates by θ, the driven blade rotates correspondingly by $\theta_{1'}$. The enclosed volume V formed by the blades, rotor, housing walls, and end covers is expressed as:

$$V = L\int_0^{\theta_{1'}} \frac{1}{2}(l_{OB_1}^2 - l_{OE_1}^2)\mathrm{d}\theta_{1'} \tag{18}$$

The instantaneous flow rate $Q(t)$ is then derived as:

$$\begin{aligned} Q(t) &= \frac{\mathrm{d}V}{\mathrm{d}t} \\ &= L\frac{\mathrm{d}}{\mathrm{d}\theta_{1'}}(\textstyle\int_0^{\theta_{1'}} \frac{1}{2}(l_{OB_1}^2 - l_{OE_1}^2)\mathrm{d}\theta_{1'})\frac{\mathrm{d}\theta_{1'}}{\mathrm{d}t} \end{aligned} \tag{19}$$

where

$$l_{OE_1} = \sqrt{\begin{array}{l} (R-e)^2 + e^2 - 2(R-e)e \\ \cdot\cos\left(\begin{array}{l} \arcsin\left(\frac{(R-e-r)\sin(\frac{\pi}{3}-\theta-\beta)}{\sqrt{(R-e-r)^2+e^2 - 2(R-e-r)e\cos(\frac{\pi}{3}-\theta-\beta)}}\right) \\ -\arcsin\left(\frac{e(R-e-r)\sin(\frac{\pi}{3}-\theta-\beta)}{(R-e)\sqrt{(R-e-r)^2+e^2 - 2(R-e-r)e\cos(\frac{\pi}{3}-\theta-\beta)}}\right) \end{array}\right) \end{array}}$$

(b) When drive blade 1 reaches position OB ($\theta \in (\pi - \alpha_0, \pi + \alpha_0)$), drive blade 1 enters the operational state. The instantaneous flow rate $Q(t)$ is then derived as:

$$Q(t) = \frac{\mathrm{d}V}{\mathrm{d}t} = L\frac{\mathrm{d}}{\mathrm{d}\theta}(\int_{\angle O_2' O O_1}^{\theta} \frac{1}{2}(l_{OB_1}^2 - l_{OE_1}^2)\mathrm{d}\theta)\frac{\mathrm{d}\theta}{dt} \tag{20}$$

where

$$l_{OE_1} = \sqrt{(R-e)^2 + e^2 + 2(R-e)e\cos(\theta + \arcsin\frac{e\sin\theta}{(R-e)}).}$$

(c) After drive blade 1 passes position OC ($\theta \in (\pi + \alpha_0, 2\pi)$), driven blade $1''$ activates. The instantaneous flow rate $Q(t)$ is then derived as:

$$Q(t) = \frac{\mathrm{d}V}{\mathrm{d}t} = L\frac{\mathrm{d}}{\mathrm{d}\theta_{1''}}(\int_0^{\theta_{1''}} \frac{1}{2}(l_{OB_1}^2 - l_{OE_1}^2)\mathrm{d}\theta_{1''})\frac{\mathrm{d}\theta_{1''}}{\mathrm{d}t} \tag{21}$$

where

$$l_{OE_1} = \sqrt{\begin{array}{l} (R-e)^2 + e^2 - 2(R-e)e \\ \cdot\cos\left(\begin{array}{l} \arcsin\left(\frac{(R-e-r)\sin(5\pi/3-\theta+\beta)}{\sqrt{(R-e-r)^2+e^2 - 2(R-e-r)e\cos(5\pi/3-\theta+\beta)}}\right) \\ -\arcsin\frac{e(R-r-e)\sin(5\pi/3-\theta+\beta)}{(R-e)\sqrt{(R-e-r)^2+e^2 - 2(R-e-r)e\cos(5\pi/3-\theta+\beta)}} \end{array}\right) \end{array}}$$

(ii) BD-BRVP Instantaneous Flow Calculation with Blade Thickness Considered

To enhance instantaneous flow rate calculation fidelity, the computational model explicitly integrates physical component geometry—with particular emphasis on blade thickness effects.

(a) When $\theta \in (0, \pi - \alpha_0)$, then $V_{\text{Ture}} = V - V_{\text{Blade}}$, and the accuracy of instantaneous flow rate $Q_{\text{Ture}}(t)$ is then derived as

$$Q_{\text{Ture}}(t) = \frac{\mathrm{d}V_{\text{Ture}}}{\mathrm{d}t} = \frac{\mathrm{d}(V - V_{\text{Blade}})}{\mathrm{d}\theta_{1'}} \frac{\mathrm{d}\theta_{1'}}{\mathrm{d}t} \tag{22}$$

(b) Drive blade 1 at critical position OB

$$Q_{\text{Ture}}(t) = \frac{\mathrm{d}(V - l_{B_1E_1}Ls)}{\mathrm{d}\theta} \frac{\mathrm{d}\theta}{\mathrm{d}t} \tag{23}$$

(c) Drive blade 1 at critical position OC

$$Q_{\text{Ture}}(t) = \frac{\mathrm{d}(V - l_{B_1E_1}Ls)}{\mathrm{d}\theta_{1''}} \frac{\mathrm{d}\theta_{1''}}{\mathrm{d}t} \tag{24}$$

4. Rotor-Driven Blade Rotor Volumetric Pump (RD-BRVP)

4.1. Structural Innovation of RD-BRVP

Performance testing of the second-generation BD-BRVP prototype confirmed persistent running instability. As established in prior analyses, the flow characteristics determined by combined effects of blade velocity variation and working chamber volume fluctuation directly influence pump stability. However, the BD-BRVP configuration incorporates both drive and driven blades, resulting in excessive pulsation of instantaneous flow rate and driveshaft torque gradient, thereby compromising operational smoothness.

To resolve these limitations, we propose the rotor-driven RD-BRVP configuration, derived from the rotationally symmetric crank-guide rod mechanism. This innovation preserves fundamental component kinematics while establishing synchronized motion among all three blades. A comprehensive comparative analysis examines

- Force-flow transmission path;
- Kinematic characteristics;
- Pressure angle distribution;
- Mechanical load behavior.

4.2. Force-Flow Transmission Path Analysis

Figure 7a schematically illustrates the force-flow transmission path in BD-BRVP. This configuration features the drive blade (bar) simultaneously actuating both sliders and the rotor (crank), with subsequent power transfer to driven blades through the rotor assembly. Conversely, Figure 7b demonstrates RD-BRVP's topology where the rotor acts as primary driver, directly actuating both sliders and all blades. This topological optimization shortens the force transmission path, significantly reducing energy losses inherent to multi-stage power transfer systems.

4.3. Comparative Analysis of Two Structural Configurations

(1) Kinematic Analysis of RD-BRVP Key Components

Applying the Section 3.1 methodology, kinematic analysis of the RD-BRVP was conducted using second-generation prototype parameters (R = 80 mm, e = 10 mm, r = 20 mm, L = 100 mm). Figure 8 compares angular velocity profiles of key components for both configurations. Crucially, the RD-BRVP achieves blade motion synchronization with sig-

nificantly attenuated velocity fluctuations. At 550 r/min driveshaft speed, the velocity variation coefficient measures 0.42 for RD-BRVP versus 0.73 for BD-BRVP—representing a 42.5% reduction in dynamic variation. Conversely, slider velocity oscillations remain negligible in both architectures.

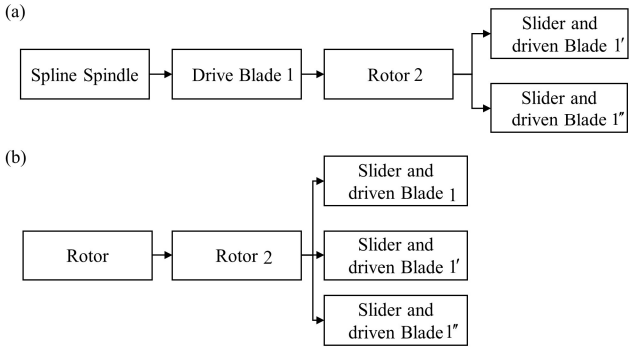


Figure 7. Force-flow transmission routes of the BRVPs: (**a**) BD-BRVP; (**b**) RD-BRVP.

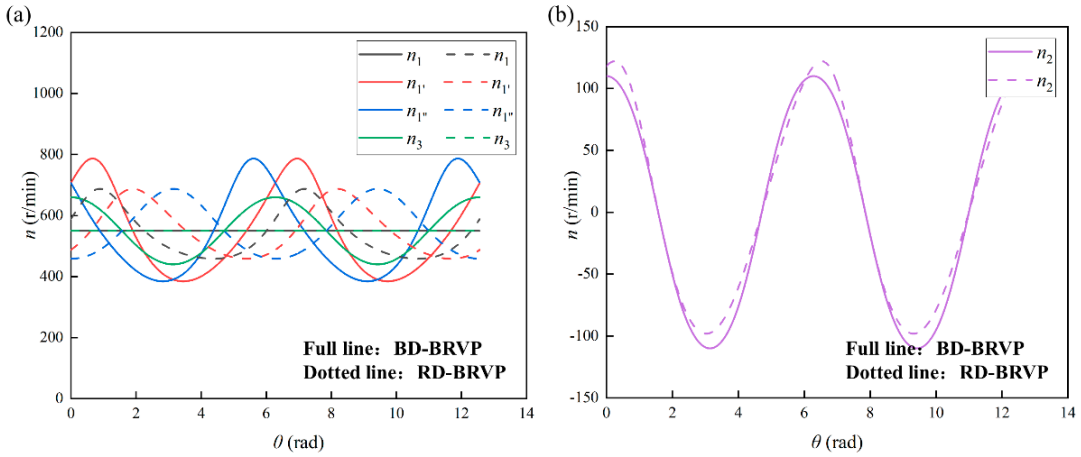


Figure 8. Comparison of rotational speeds of the main components of BRVPs: (**a**) blades and rotors; (**b**) sliders.

(2) Pressure Angle Characteristics

For the BD-BRVP (Figure 9), the non-zero pressure angle $\alpha = \angle O_1O_2O = \arcsin(\lambda \sin\theta)$ exists at position O_2 for the crank (rotor), while the pressure angles at positions O_2' and O_2'' remain zero for the driven blades. Conversely, the RD-BRVP maintains zero pressure angles across all blades throughout its operational cycle. This fundamental design improvement enables superior force transmission efficiency in the RD-BRVP configuration.

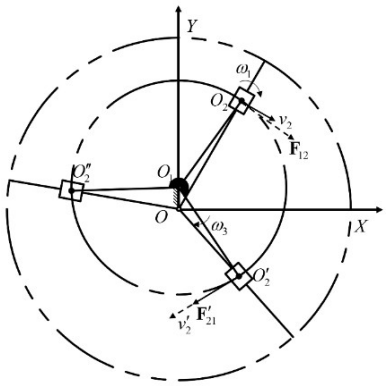


Figure 9. Pressure angle of the BRVP mechanism.

(3) Mechanical Behavior Comparison

The RD-BRVP exhibits mechanical loading characteristics similar to the BD-BRVP, with the fundamental distinction that driveshaft torque M acts directly on the crank-rotor assembly. Applying the Section 3.1 analytical framework, Figure 10 compares driveshaft torque and power consumption for both configurations under identical parameters. The RD-BRVP achieves an 18.76% reduction in torque fluctuation rate relative to the BD-BRVP. At matched operating conditions (Δp = 1 MPa, ω = 550 r/min), RD-BRVP demonstrates an 11% reduction in theoretical peak power consumption (9.95 kW vs. 11.05 kW, Figure 10b). This efficiency improvement enables downsizing of power transmission components, reducing system mass and cost.

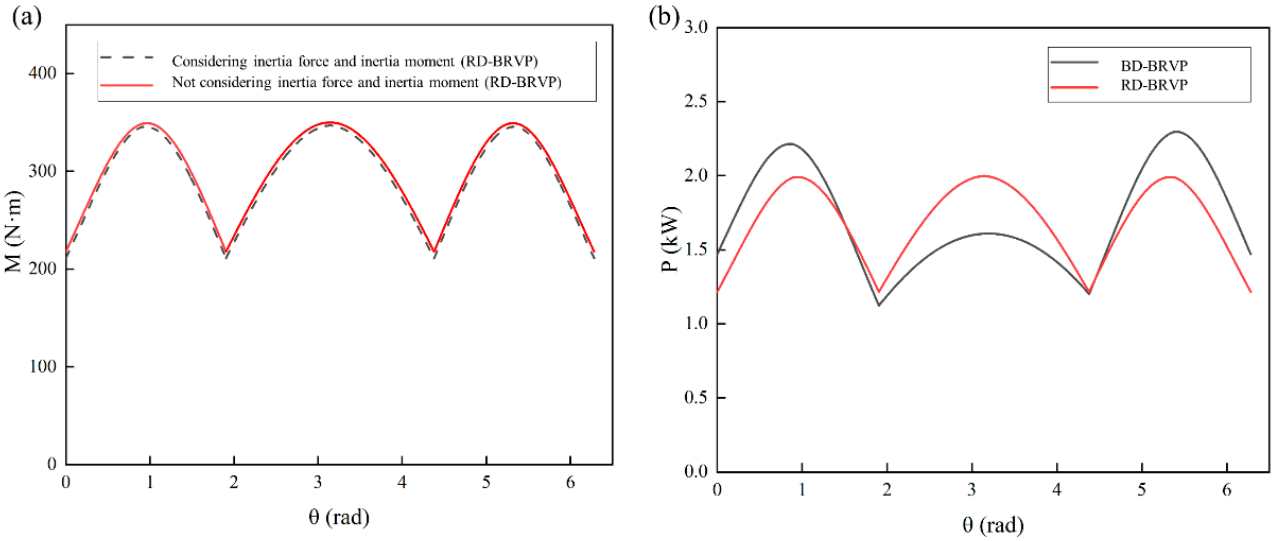


Figure 10. Mechanical characteristics of the main shaft of the RD-BRVP: (**a**) driving moment; (**b**) comparison of power consumption of RD-BRVP with the BD-BRVP.

(4) Instantaneous Flow Comparison

Instantaneous flow characteristics obtained from the analytical methodology in Section 3.2 are presented in Figure 11. The RD-BRVP (red curve) exhibits a flow pulsation rate of 42.95%—representing a 20.75% reduction relative to the BD-BRVP's 63.7% (black curve) at 550 r/min—confirming superior operational smoothness.

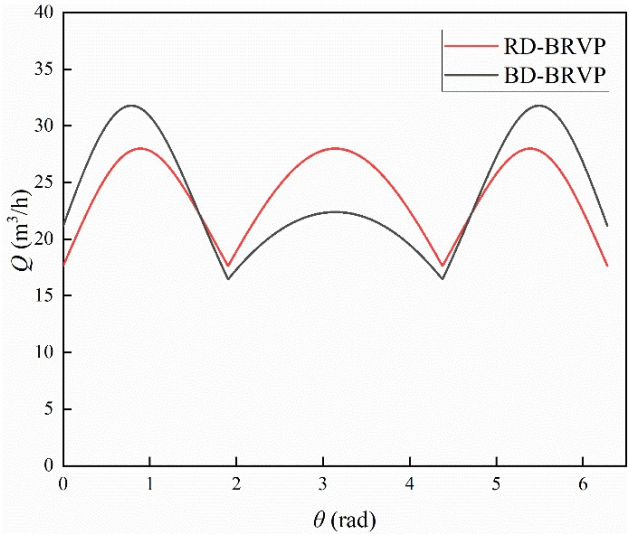


Figure 11. Comparison of instantaneous flow curves of the BRVP.

(5) Flow Pulsation Rate Quantification

Applying the Section 3.2 methodology, the RD-BRVP flow pulsation rate is formulated as

(i) When the blade angle at $\theta_0 = \frac{1}{2}\left(\pi - \arcsin\left(\frac{\sqrt{3}}{2\sqrt{\lambda^2+1-\lambda}}\right)\right)$, $\frac{dQ(t)}{dt} = 0$, the instantaneous flow rate $Q(t)$ attains its maximum value Q_{max}:

$$Q_{max} = \frac{\pi n L}{15} e(R-e) \frac{\cos\left(\arcsin\frac{\lambda \sin(\frac{\pi}{3}-\theta_0-\beta_1)}{\sqrt{\lambda^2+1-2\lambda\cos(\frac{\pi}{3}-\theta_0-\beta_1)}}\right)}{\sqrt{\lambda^2+1-2\lambda\cos(\frac{\pi}{3}-\theta_0-\beta_1)}} \tag{25}$$

where

$$\frac{\pi}{3} - \theta_0 - \beta_1 = \frac{\pi}{3} - \frac{1}{2}\left(\pi - \arcsin\left(\frac{\sqrt{3}}{2\sqrt{\lambda^2+1-\lambda}}\right)\right) - \arcsin\left(\lambda\cos\left(\arcsin\left(\frac{\sqrt{3}}{2\sqrt{\lambda^2+1-\lambda}}\right)\right)\right)$$

(ii) When the blade angle at $\theta = \pi - \arcsin(\frac{\sqrt{3}\lambda}{2\sqrt{\lambda^2+1-\lambda)}})$, the instantaneous flow rate Q(t) attains its minimum value Q_{min}:

$$\begin{aligned} Q_{min} = {} & \tfrac{\pi n L}{30} e(R-e)\left(1+\cos\left(\begin{array}{c}\arcsin\left(\frac{\sqrt{3}}{2\sqrt{\lambda^2+1-\lambda}}\right) \\ -\arcsin\left(\frac{\sqrt{3}e}{2(R-e)\sqrt{\lambda^2+1-\lambda}}\right)\end{array}\right)\right) \\ & \cdot \frac{\cos\left(\arcsin\frac{\lambda\sin(\frac{\pi}{3}-\theta-\beta)}{\sqrt{1+\lambda^2-2\lambda\cos(\frac{\pi}{3}-\theta-\beta)}}\right)}{\sqrt{1+\lambda^2-2\lambda\cos(\frac{\pi}{3}-\theta-\beta)}} \end{aligned} \tag{26}$$

where

$$\frac{\pi}{3} - \theta - \beta = \arcsin\left(\frac{\sqrt{3}}{2\sqrt{\lambda^2+1-\lambda}}\right) - \arcsin\left(\frac{\sqrt{3}\lambda}{2\sqrt{\lambda^2+1-\lambda}}\right) - \frac{2\pi}{3}$$

As illustrated in Figure 12, flow pulsation rates for both BRVP configurations are compared across varying structural parameters, with solid lines denoting BD-BRVP and dashed lines representing RD-BRVP. The parametric trends were quantified through polynomial regression (Equations (27) and (28)), establishing their functional dependencies. Comparative equation analysis reveals a reduced first-order coefficient in the RD-BRVP model, resulting in systematic downward shifting of its characteristic curve. Consequently, under identical parametric conditions, the RD-BRVP configuration exhibits consistently lower flow pulsation rates than the BD-BRVP throughout the investigated design space.

$$\delta = \begin{cases} 2.91\times10^{-4}R^2 - 0.058R + 3.41 & 60 \le R \le 100 \\ 2.51\times10^{-4}r^2 + 5.68\times10^{-4}r + 0.54 & 10 \le r \le 30 \\ 0.0022e^2 + 0.0098r + 0.33 & 8 \le e \le 12 \end{cases} \tag{27}$$

$$\delta = \begin{cases} 1.71\times10^{-4}R^2 - 0.034R + 2.03 & 60 \le R \le 100 \\ 1.57\times10^{-4}r^2 - 5.34\times10^{-5}r + 0.38 & 10 \le r \le 30 \\ 0.0015e^2 - 0.0027r + 0.32 & 8 \le e \le 12 \end{cases} \tag{28}$$

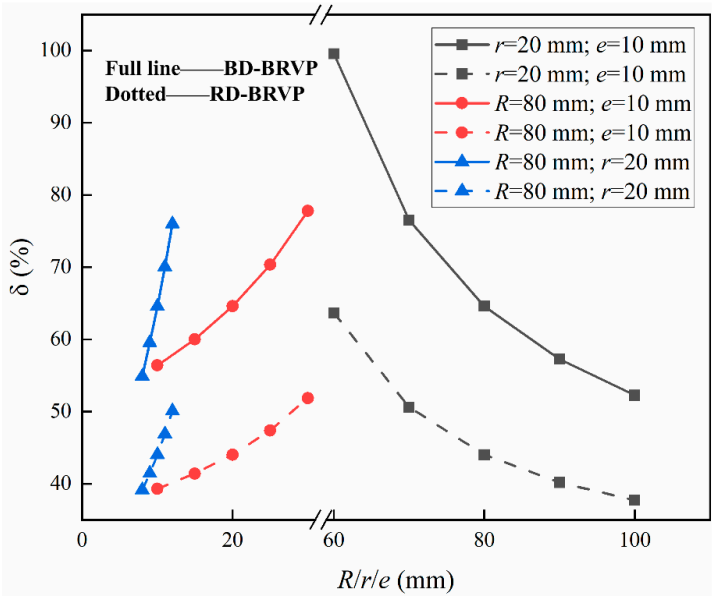


Figure 12. Comparison of flow pulsation rates between two motion schemes of the BRVPs with different parameters.

5. Experimental Validation of BRVP Prototype Performance

5.1. Implementation of BD-BRVP Configuration

The 3D model and physical prototype of RD-BRVP are presented in Figure 13 [18,19].

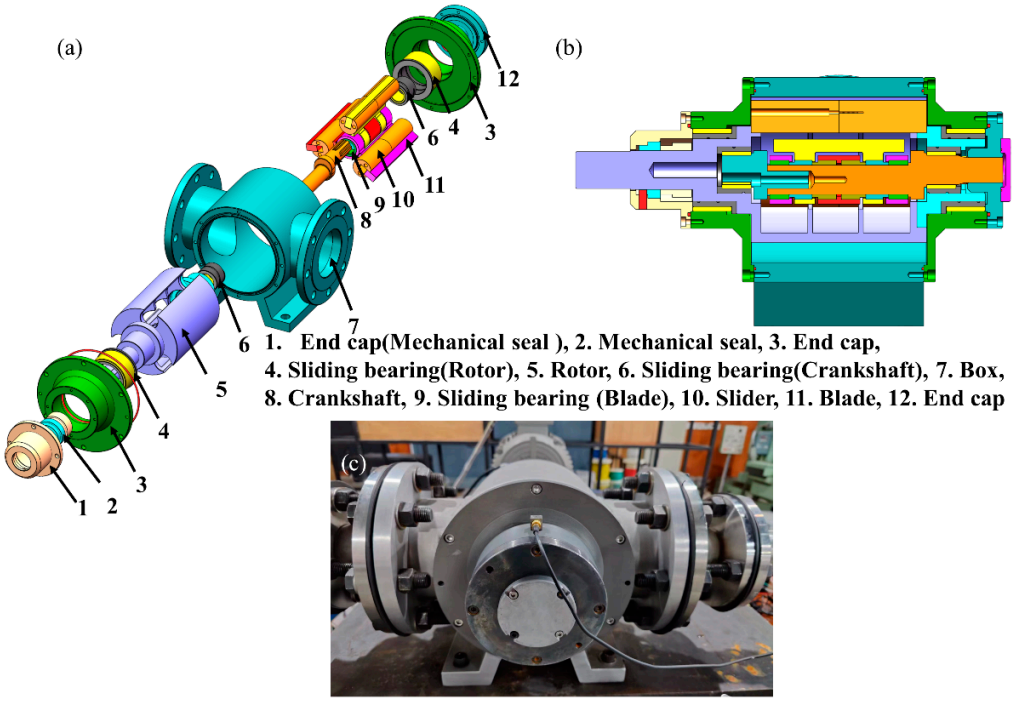


Figure 13. RD-BRVP: (**a**) explosion model; (**b**) section model; (**c**) prototype.

The fundamental structural and kinematic distinction between the two pump configurations resides in the power input topology. In the BD-BRVP (Figure 14a), a spline-coupled driveshaft directly interfaces with the drive blade, which acts as the prime mover to actuate the sliders and rotor. In contrast, the RD-BRVP (Figure 14b) employs the rotor as the primary driving element, transmitting torque directly to all three blades and sliders in parallel. This kinematic inversion simplifies the power transmission path and improves

mechanical efficiency. As further illustrated in Figure 14b, the crankshaft of the RD-BRVP is integrated within the rotor, with eccentricity e as the center-to-center distance between the main journal and connecting rod journal. This configuration enables precise orbital motion of the blades, while the crankshaft is secured against rotation via a splined rear cover, resulting in a fundamentally distinct transmission mechanism compared to the blade-driven BD-BRVP design.

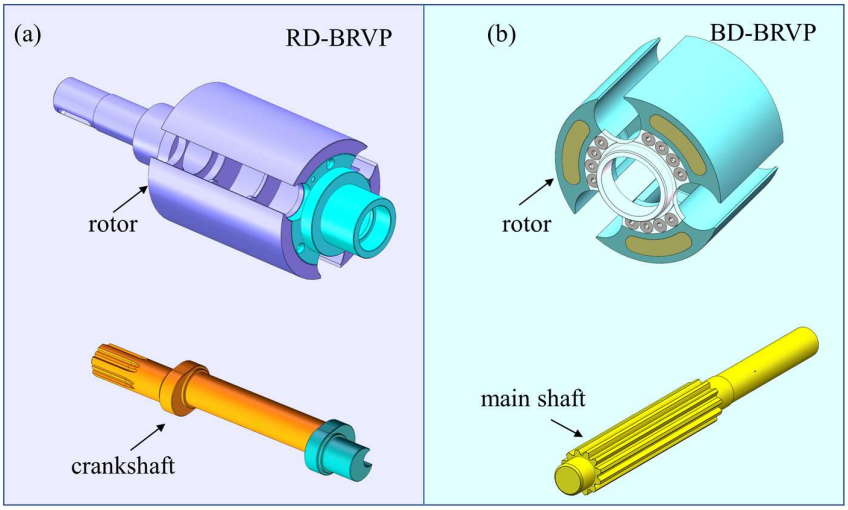


Figure 14. Structural differences between the rotor and main shaft in both configurations: (**a**) BD-BRVP; (**b**) RD-BRVP.

5.2. BRVP Performance Test System

A dedicated performance evaluation platform was constructed in strict compliance with the Chinese National Standard GB/T 3216-2016 (Rotodynamic pumps-Hydraulic performance acceptance tests-Grades 1, 2, and 3) [20], as illustrated in Figure 15. Key instrumentation included

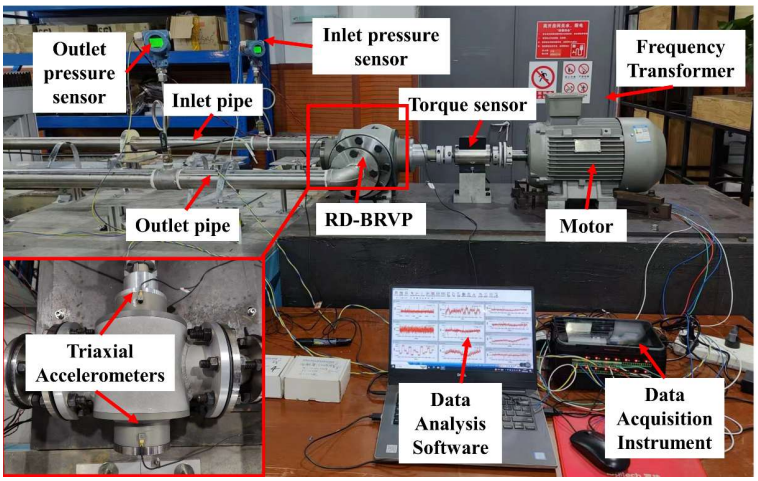


Figure 15. BRVP performance experimental platform.

- Torque sensor (Range: 0–±100 N·m, Accuracy: ±0.5%);
- Speed sensor (0–3000 r/min, Accuracy: ±1 r/min);
- Pressure sensor (Range: −100 kPa–2 MPa, Accuracy: ±0.1%);
- Turbine flowmeter (Range: >1 m^3/h, Accuracy: 0.5%);
- Triaxial accelerometers (Range: 0–10.2 g, Accuracy: ±2.5% (2500 < f ≤ 10,000 Hz); ±5% (10,000 < f ≤ 20,000 Hz)).

Key operational parameters—including rotational speed, torque, inlet/outlet pressures, volumetric flow rate, head, and vibration signatures—were continuously recorded and subsequently analyzed to generate performance curves.

To ensure the reliability of the experimental data, a comprehensive uncertainty analysis was conducted. The standard uncertainties of the primary sensors, as obtained from calibration certificates, are as follows: torque sensor, ±0.5%; speed sensor, ±1 r/min; pressure sensor, ±0.1%; turbine flowmeter, ±0.5%; triaxial accelerometer, ±2.5% (2500 < f ≤ 10,000 Hz) and ±5% (10,000 < f ≤ 20,000 Hz). Using the root-sum-square (RSS) method for uncertainty, the uncertainties for the key performance parameters were calculated to be ±0.53% for the flow rate, ±0.48% for the pressure head. These negligible uncertainty levels confirm that the measured performance improvements are statistically significant and attributable to the design changes rather than measurement errors.

5.3. Performance Parameter Testing

(1) Hydraulic Loss Calculation

To ensure accurate assessment of pump efficiency, both frictional and minor (local) head losses were accounted for:

(i) Frictional Head Loss (h_c)

Calculated using the Hazen-Williams equation [21]:

$$h_c = \frac{10.67 Q^{1.852} L_P}{C_h^{1.852} d^{4.87}} \tag{29}$$

where

h_c = frictional head loss (m)

L_p = pipe length (m)

D = inner diameter (m)

Q = flow rate (m^3/s)

C_h = Hazen-Williams coefficient (120–140 for new steel/ductile iron; 100–120 for aged systems).

(ii) Minor Head Loss (h_ζ)

This is expressed as

$$h_\zeta = \zeta \frac{v^2}{2g} \tag{30}$$

where

h_ζ = minor head loss (m)

ζ = resistance coefficient (experimentally/empirically determined)

(2) BD-BRVP Performance Testing

Performance tests were conducted using nozzles with different diameters (50, 40, 32, 25, 20, and 15 mm), with motor speed regulated by a variable-frequency drive. At a low rotational speed of 97.7 r/min and using a large 40-mm diameter nozzle, the instantaneous flow profile (Figure 16a) exhibited a mean flow rate of 3.97 m^3/h with a fluctuation of 1.16%. Consistent with the analysis in Section 3.2, torque signals (Figure 16b,c) were utilized to validate flow pulsation characteristics. At 97.72 r/min, the experimental torque fluctuation rate reached 64.34%, which closely matched the theoretical value of 63.21%, with a deviation of only 1.13%.

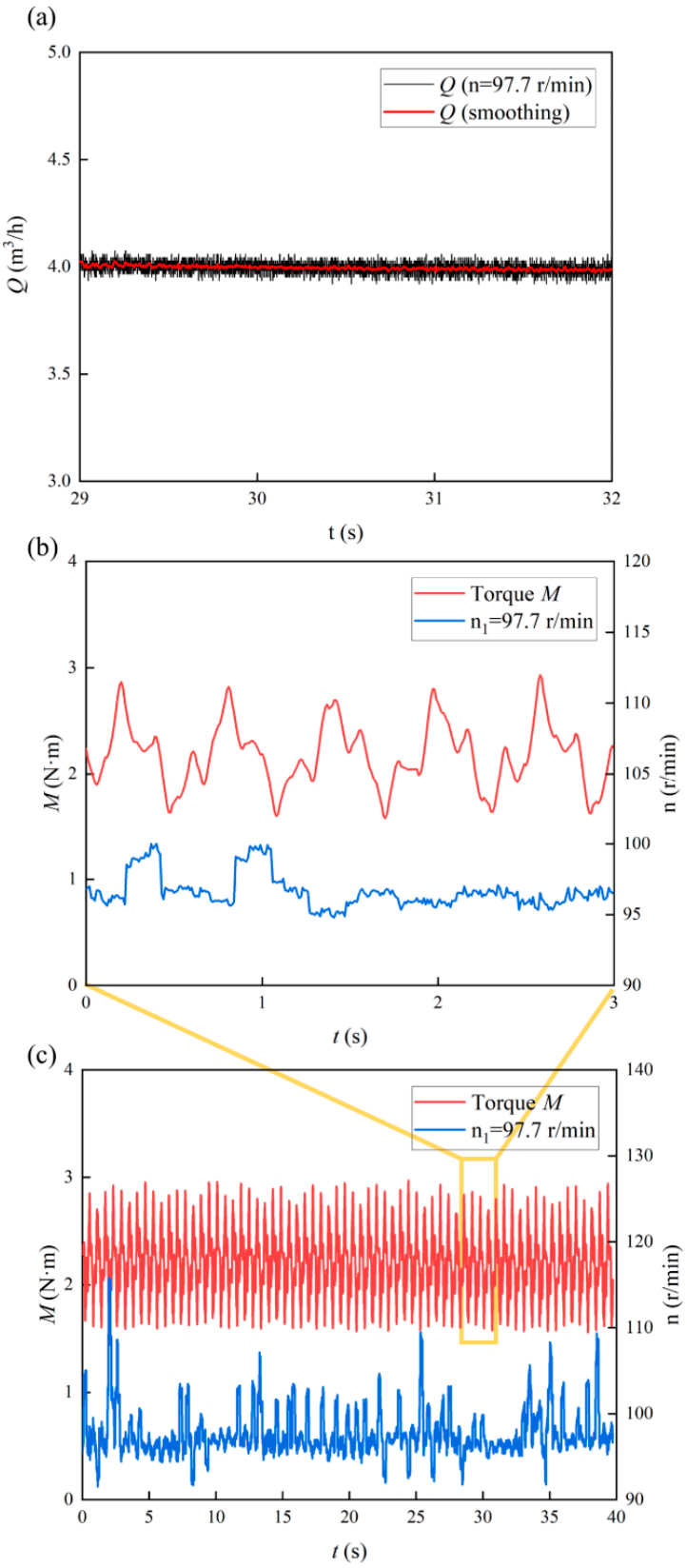


Figure 16. Spindle torque curve of BD-BRVP with time (n_1 = 97.7 r/min): (**a**) instantaneous flow, (**b**,**c**) spindle torque.

(3) RD-BRVP Performance Testing

For the RD-BRVP operating at 204.6 r/min with a 50-mm nozzle, the experimentally measured torque fluctuation rate was 48.65% (see Figure 17b). This value deviates by 5.7%

from the theoretically predicted value of 42.95%. The periodic torque profiles (Figure 17a) exhibited three distinct peaks per cycle, validating the theoretical predictions as expected.

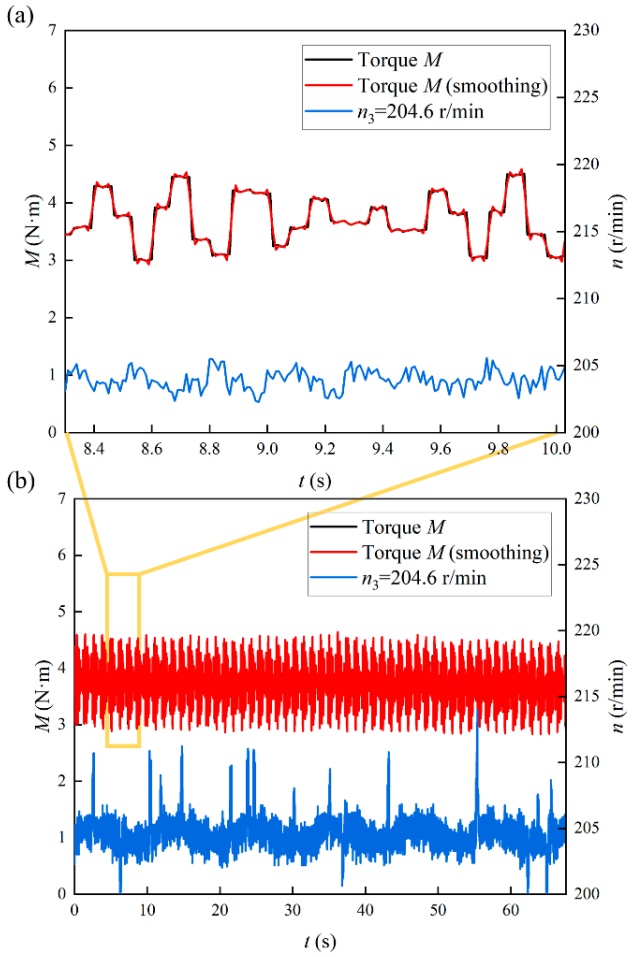


Figure 17. Spindle torque curve of RD-BRVP with time (n_3 = 204.6 r/min): (**a**,**b**) spindle torque.

5.4. Vibration Characteristics

Vibration signals were recorded at predefined measurement points (see Figure 18).

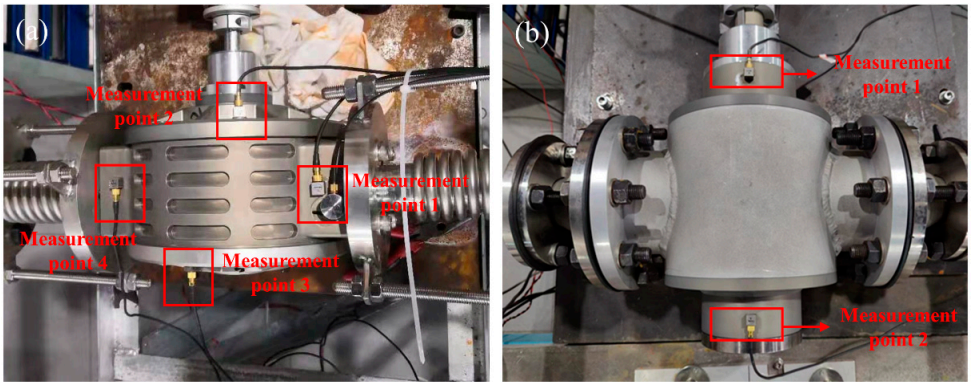


Figure 18. Vibration measurement points: (**a**) BD-BRVP; (**b**) RD-BRVP.

In accordance with GB/T 29531-2013 (Pump Vibration Measurement and Evaluation Methods) [22], was evaluated using the root mean square (RMS) velocity:

$$V_{rms} = \sqrt{\frac{1}{T}\int_0^T v^2(\mathrm{t})\mathrm{dt}} \tag{31}$$

where

V_{rms} = RMS velocity (mm/s)

T = sampling duration (s)

$v(t)$ = time-domain velocity (mm/s)

At operating speeds of 406 r/min for the BD-BRVP and 900 r/min for the RD-BRVP, the peak vibration velocity (V_{rms}) reached 19.29 mm/s (measured at Point 4-Y on the BD-BRVP) and 1.71 mm/s (measured at Point 1-Z on the RD-BRVP), as shown in Figure 19. According to the ISO 10816-7 classification standard [23] (applying to the frequency range of 10 Hz–1 kHz), the BD-BRVP exhibited Grade D vibration severity (corresponding to 28 mm/s), while the RD-BRVP achieved Grade B vibration severity (1.8 mm/s). The RD-BRVP's measured vibration level was significantly below the 2.8 mm/s threshold specified for Class I horizontal pumps (with Center Height H < 225 mm and rotational speed n < 1800 r/min).

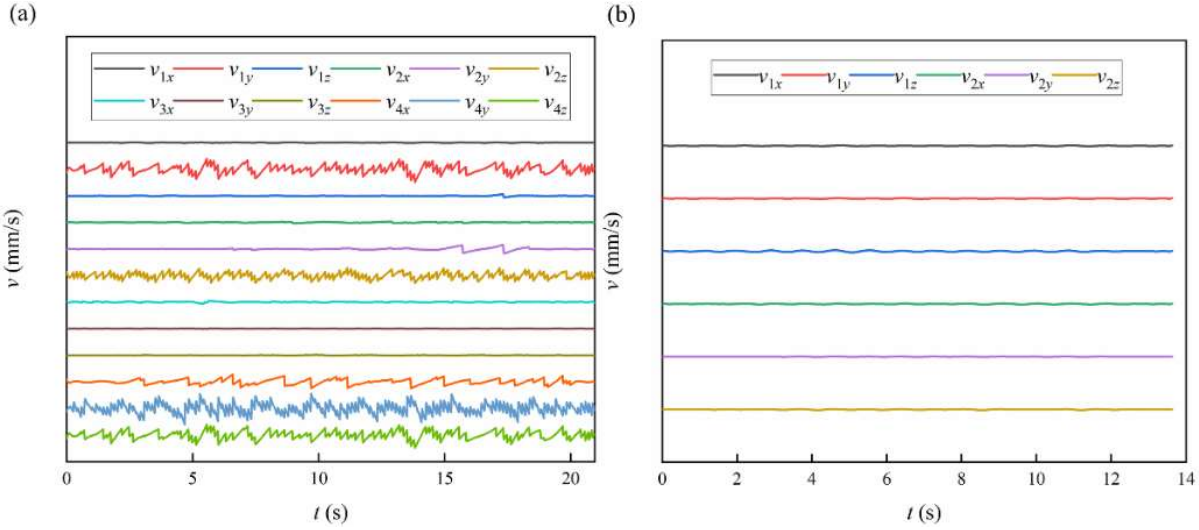


Figure 19. Vibration speed: (**a**) BD-BRVP; (**b**) RD-BRVP.

6. Conclusions

Building upon the kinematics of a rotationally symmetric crank-guide rod mechanism, this study presents a comprehensive analysis of the structural configuration, operational principles, mechanical systems, and flow characteristics of the Blade Rotor Volumetric Pump (BRVP). To address the running instability identified in the blade-driven BD-BRVP configuration, a redesigned rotor-driven RD-BRVP is proposed. Comprehensive comparative analyses of force-flow transmission paths, pressure angles, mechanical behavior, and flow dynamics yield the following principal conclusions:

(1) Structural Advantages of BRVP

The dual-centering configuration ensures the reliability of the reciprocating motion of the blades relative to the rotor. Concurrently, the clearance sealing mechanism between blade tips and housing walls achieves low leakage rates and minimal wear. The periodic variation in working chamber volume, coupled with efficient fluid–blade interaction, facilitates the conversion of mechanical energy into hydraulic energy.

(2) Performance Superiority of RD-BRVP

The optimized force transmission path in the RD-BRVP delivers significant performance gains: a 42.5% reduction in blade velocity fluctuations and a 20.75% decrease in instantaneous flow pulsation (under parameters R = 80 mm, e = 10 mm, r = 20 mm, L = 100 mm). Furthermore, the theoretical peak power consumption is reduced by 11%,

enabling the selection of more cost-effective power units. Experimental validation confirms markedly enhanced stability, with vibration severity reduced from Grade D (28 mm/s) to Grade B (1.8 mm/s).

This research establishes a systematic framework correlating critical structural parameters with performance characteristics in BRVP-type centering rotor pumps. Through rigorous theoretical modeling and experimental validation, the RD-BRVP configuration demonstrates substantial improvements in operational smoothness and energy efficiency. These advancements significantly elevate the technological maturity of this pump architecture and lay the groundwork for its practical implementation in industrial fluid systems.

Author Contributions: Conceptualization, Y.H. and B.L.; Data curation, Y.H., F.Z. and L.F.; Formal analysis, Y.H. and F.Z.; Funding acquisition, B.L., T.S. and X.H.; Investigation, Y.H., F.Z. and L.F.; Methodology, Y.H. and F.Z.; Project administration, B.L. and T.S.; Resources, B.L. and T.S.; Supervision, B.L., T.S. and X.H.; Validation, Y.H. and F.Z.; Visualization, Y.H., F.Z. and L.F.; Writing—original draft, Y.H., F.Z. and X.H.; Writing—review & editing, Y.H., F.Z. and T.S. All authors have read and agreed to the published version of the manuscript.

Funding: The APC was funded by the China Aerodynamics Research and Development Center.

Data Availability Statement: The original contributions presented in this study are included in the article. Further inquiries can be directed to the corresponding author.

Conflicts of Interest: The authors declare no conflicts of interest.

Nomenclature

R	radius of driven blades (mm)	M_{I1}	inertial moment of the drive blade 1 (N·m)
O	rotational centers of blades (mm)	F_{I1y}	inertial force along the y-direction at the center of mass of the drive blade 1 (N)
e	eccentricity (mm)	v_{S_1y}	velocity along the y-direction at the center of mass of the drive blade 1 (m/s)
R-e	radius of rotor (mm)	G_1'	gravity at the center of mass of the driven blade 1′ (N)
O_1	rotational centers of rotor	n_1	rotational speed of drive blades (r/min)
O_2, O_2', O_2''	rotation center of slider	q	the displacement (mm^3/r)
r	radius of sliders (rad)	L	axial length of pump (mm)
1	drive blade	S_{BECF}	area of the shaded area enclosed by B, E, C, and F (mm^2)
1′	driven blade	$\overline{Q}$	theoretical mean flow rate (m^3/h)
1″	driven blade	V	enclosed volume formed by the blades, rotor, housing walls, and end covers (mm^3)
φ_1	angular displacements of drive blade 1 (rad)	$\theta_{1'}$	angle at which the driven blade has rotated (rad)
φ_3	angular displacements of rotor 3 (rad)	$Q(t)$	instantaneous flow rate (m^3/h)
ω_3	angular velocity of the rotor 3 (rad/s)	$Q_{\mathrm{Ture}}(t)$	accuracy of instantaneous flow rate (m^3/h)
l_{OO_2}	distance between O_1 and O_2 (mm)	s	thickness of blade (mm)
ω_1'	angular velocities of driven blade 1′ (rad/s)	α	non-zero pressure angle (rad)
ω_1''	angular velocities of driven blade 1″ (rad/s)	Δp	difference pressure between inlet and outlet (MPa)
φ_3'	angular displacements of rotor 3 (rad) (corresponding to 1′)	δ	flow pulsation rates
φ_1'	angular displacements of drive blade 1′ (rad)	f	frequency (Hz)
$l_{OO_2'}$	distance between O and O_2' (mm)	h_{c}	frictional head loss (m)
φ_3''	angular displacements of rotor 3 (rad) (corresponding to 1″)	L_{p}	pipe length (m)
φ_1''	angular displacements of drive blade 1″ (rad)	D	inner diameter (m)
$l_{OO_2''}$	distance between O and O_2'' (mm)	C_{h}	Hazen-Williams coefficient

β	relative angular displacement between sliders and their grooves	h_ζ	minor head loss (m)
t	time	ζ	resistance coefficient
ω_2	relative angular velocity between sliders and their grooves	V_{rms}	RMS velocity (mm/s)
θ	angle at which the drive blade has rotated (rad)	T	sampling duration (s)
M'_{r1}	working resistance torque acting on driven blade	H	center height of the pump (mm)
M	driveshaft driving torque		

Abbreviations

The following abbreviations are used in this manuscript:

BD-BRVP	Blade-Driven Blade Rotor Volumetric Pump
RD-BRVP	Rotor-Driven Blade Rotor Volumetric Pump
CFD	Computational Fluid Dynamics
RSS	Root-Sum-Square

References

1. Intriago Zambrano, J.C.; Michavila, J.; Arenas Pinilla, E.; Diehl, J.C.; Ertsen, M.W. Water lifting water: A comprehensive spatiotemporal review on the hydro-powered water pumping technologies. *Water* **2019**, *11*, 1677. [CrossRef]
2. Hussin, N.S.M.; Gamil, S.A.; Amin, N.A.M.; Safar, M.J.A.; Majid, M.S.A.; Kazim, M.N.F.M.; Nasir, N.F.M. Design and analysis of hydraulic ram water pumping system. *J. Phys. Conf. Ser.* **2017**, *908*, 012052. [CrossRef]
3. Peng, S.; Yang, H.; Hao, J.; Ma, B.; Wu, Q.; Wang, Y. Intelligent real-time pump scheduling in water distribution networks based on graph convolutional networks. *Water Res. X* **2025**, *28*, 100388. [CrossRef]
4. Blinco, L.J.; Simpson, A.R.; Lambert, M.F.; Auricht, C.A.; Hurr, N.E.; Tiggemann, S.M.; Marchi, A. Genetic algorithm optimization of operational costs and greenhouse gas emissions for water distribution systems. *Procedia Eng.* **2014**, *89*, 509–516. [CrossRef]
5. Capurso, T.; Bergamini, L.; Torresi, M. A new generation of centrifugal pumps for high conversion efficiency. *Energy Convers. Manag.* **2022**, *256*, 115341. [CrossRef]
6. Zhao, S.; Tang, H.; Liu, Y.; Ren, Y.; Wu, D. Flow characteristics of asymmetric plunger pairs in high-pressure plunger pumps. *J. Tribol.* **2025**, *147*, 044102. [CrossRef]
7. Suo, X.; Jiang, Y.; Wang, W. Hydraulic axial plunger pump: Gaseous and vaporous cavitation characteristics and optimization method. *Eng. Appl. Comput. Fluid Mech.* **2021**, *15*, 712–726. [CrossRef]
8. Shukla, P.K.; Mishra, R.; Tewari, R.P. Analysis of rotary ventricular assist devices using CFD technique—A review. *Proc. Inst. Mech. Eng. Part E J. Process Mech. Eng.* **2023**, *237*, 1036–1063. [CrossRef]
9. Siddique, M.H.; Afzal, A.; Samad, A. Design optimization of the centrifugal pumps via low fidelity models. *Math. Probl. Eng.* **2018**, *2018*, 3987594. [CrossRef]
10. Liang, Y.; Wang, W.; Zhang, Z.; Xing, H.; Wang, C.; Zhang, Z.; Guan, T.; Gao, D. Effect of material selection and surface texture on tribological properties of key friction pairs in water hydraulic axial piston pumps: A review. *Lubricants* **2023**, *11*, 324. [CrossRef]
11. Rode, B.R.; Khare, R. A review on development in design of multistage centrifugal pump. *Adv. Comput. Des.* **2021**, *6*, 43–53. [CrossRef]
12. Ali, A.; Yuan, J.; Deng, F.; Wang, B.; Liu, L.; Si, Q.; Buttar, N.A. Research progress and prospects of multi-stage centrifugal pump capability for handling gas–liquid multiphase flow: Comparison and empirical model validation. *Energies* **2021**, *14*, 896. [CrossRef]
13. Díez, J.-L.; Masip-Moret, V.; Santafé-Moros, A.; Gozálvez-Zafrilla, J.M. Comparison of artificial intelligence control strategies for a peristaltically pumped low-pressure driven membrane process. *Membranes* **2022**, *12*, 883. [CrossRef] [PubMed]
14. Zhou, Y.; Pavesi, G.; Yuan, J.; Fu, Y. A review on hydrodynamic performance and design of pump-Jet: Advances, challenges and prospects. *J. Mar. Sci. Eng.* **2022**, *10*, 1514. [CrossRef]
15. Zhang, P.; Wei, X.; Yan, L.; Xu, H.; Yang, T. Review of recent developments on pump-assisted two-phase flow cooling technology. *Appl. Therm. Eng.* **2019**, *150*, 811–823. [CrossRef]
16. Hsieh, C.-F. Flow Characteristics of Gerotor Pumps With Novel Variable Clearance Designs. *J. Fluids Eng.* **2015**, *137*, 041107. [CrossRef]
17. Li, M.; Foss, R.; Stelson, K.A.; Van de ven, J.D.; Barth, E.J. Design, Dynamic Modeling, and Experimental Validation of A Novel Alternating Flow Variable Displacement Hydraulic Pump. *IEEE/ASME Trans. Mechatron.* **2019**, *24*, 1294–1305. [CrossRef]

18. Zhao, F.; He, Y.; Lin, B.; Wang, Y.; Sui, T.; Lin, W.; Fang, L.; Liao, M. Investigation of wear mechanisms in multi-scale short carbon fiber reinforced PTFE composites for blade rotor volumetric pumps in variable lubrications. *Polym. Compos.* **2025**, 1–17. [CrossRef]
19. He, Y.; Lin, B.; Wang, Y.; Zhao, F.; Yan, S.; Ning, G.; Bao, X.; Li, H.; Sui, T. Hybrid reinforcing effect of multi-scale short carbon fibers on the wear resistance of PTFE composites: Self-reconstruction and stress transmission. *Tribol. Int.* **2024**, *194*, 109510. [CrossRef]
20. *GB/T 3216-2016*; Rotodynamic Pumps—Hydraulic Performance Acceptance Tests—Grades 1, 2, and 3. Standards Press of China: Beijing, China, 2016.
21. Liou, C.P. Limitations and proper use of the Hazen-Williams equation. *J. Hydraul. Eng.* **1998**, *124*, 951–954. [CrossRef]
22. *GB/T 29531-2013*; Methods of Measuring and Evaluating Vibration of Pumps. Standards Press of China: Beijing, China, 2013.
23. *ISO 10816-7:2009*; Mechanical Vibration—Evaluation of Machine Vibration by Measurements on Non-Rotating Parts—Part 7: Rotodynamic Pumps for Industrial Applications, Including Measurements on Rotating Shafts. International Organization for Standardization: Geneva, Switzerland, 2009.

Disclaimer/Publisher's Note: The statements, opinions and data contained in all publications are solely those of the individual author(s) and contributor(s) and not of MDPI and/or the editor(s). MDPI and/or the editor(s) disclaim responsibility for any injury to people or property resulting from any ideas, methods, instructions or products referred to in the content.